

A High-Throughput Search for Stable and Magnetically Robust Fe_3XY_2 Monolayers

Soheil Ershadrad¹ and Biplab Sanyal¹

Department of Physics and Astronomy, Uppsala University, Box-516, 75120 Uppsala, Sweden

(*Electronic mail: biplab.sanyal@physics.uu.se)

(Dated: 3 September 2025)

We present first principles exploration of 529 Fe_3XY_2 compounds, where X and Y elements are selected from the p -block of the periodic table. Out of the entire set, 31 compounds satisfy all criteria for energetic, dynamic, mechanical, and thermal stability. Our analysis reveals several key trends: halide-containing systems exhibit the highest average magnetic moments and the highest magnetic transition temperatures, highlighting their potential for room-temperature spintronic applications. The majority of stable compounds display perpendicular magnetic anisotropy (PMA), with Fe_3SiTe_2 exhibiting the strongest PMA among all candidates. Exchange interactions are found to be governed by a dual mechanism, direct exchange between nearest-neighbor Fe atoms and indirect, p -orbital-mediated exchange for second-nearest neighbors and beyond. Notably, four compounds have non-centrosymmetric crystal structures and exhibit finite spiralization constants. Among them, Fe_3AsBr_2 is predicted to host Néel-type skyrmions even at zero external magnetic field, as confirmed by micromagnetic simulations. These findings offer a roadmap for experimental realization of novel 2D ferromagnets with enhanced functionalities.

I. INTRODUCTION

Two-dimensional (2D) magnets have emerged as promising candidates for next-generation spintronic devices, largely due to their high surface-to-volume ratio and tunable physical properties. The reduced dimensionality in these systems leads to quantum confinement effects, often resulting in electronic and magnetic behaviors that differ markedly from their bulk counterparts^{1,2}. The successful synthesis of monolayer CrI_3 and CrGeTe_3 in 2017^{3,4} sparked intense interest in the exploration and development of 2D magnetic materials. However, one of the major limitations of semiconducting 2D magnets such as CrI_3 and CrGeTe_3 is their relatively low magnetic transition temperatures (typically in the range of 40–60 K), which severely restricts their practical applications in room-temperature technologies. In contrast, metallic 2D magnets benefit from long-range exchange interactions, which significantly enhance their magnetic transition temperatures⁵. A notable breakthrough was the synthesis of monolayer Fe_3GeTe_2 in 2018⁶, which exhibits a Curie temperature of approximately 250 K. This discovery marked a pivotal step toward the realization of practical, room-temperature applications of 2D magnetic materials in devices. Subsequent studies revealed that other members of the Fe_nGeTe_2 family with higher Fe concentrations, such as Fe_4GeTe_2 and Fe_5GeTe_2 , exhibit even higher Curie temperatures^{7–9}. Furthermore, doping with 3d transition metals has been shown to further enhance the magnetic transition temperature, offering additional tunability for spintronic applications^{10,11}. To date, several functional spintronic devices, such as spin valves and spin-orbit torque devices, have been successfully fabricated using Fe_nGeTe_2 thin films^{12–14}.

The recent synthesis of Fe_3GaTe_2 monolayers¹⁵, exhibiting a magnetic transition temperature of 300 K, suggests that elemental substitution within the Fe_3XY_2 framework can be an effective strategy for designing superior 2D magnets.

In addition to limitations in magnetic transition temperatures, both Fe_3GeTe_2 and Fe_3GaTe_2 are known to be highly air-sensitive, with surface oxidation significantly degrading their magnetic properties¹⁶. Furthermore, based on the periodic table of elemental scarcity¹⁷, tellurium availability is projected to face serious depletion within the next 100 years. Therefore, the prediction and synthesis of Te-free two-dimensional magnets are crucial for ensuring long-term viability in industrial applications.

High-throughput (HTP) screening has emerged as a powerful strategy for systematically identifying promising candidates in materials discovery. While several large-scale materials databases exist, they primarily focus on bulk (3D) compounds^{18,19}. Consequently, most existing HTP studies rely on data mining from these databases, which limits the systematic exploration of 2D magnets to few compounds that are already known or previously reported^{20,21}. We address this gap by developing a custom HTP platform that enables the autonomous generation, structural optimization, and magnetic property modeling of a wide range of compounds. Similar HTP methodologies have proven successful in other material classes, such as MAX phases and MXenes^{22–24}. By applying a similar framework to 2D magnets, we not only uncover trends and hidden correlations that are difficult to detect from studies of individual compounds, but also generate a rich dataset that can support future data-driven approaches, including machine learning-based materials prediction.

In this study, we employ HTP first-principles calculations to explore 529 possible Fe_3XY_2 compounds in search of robust and stable two-dimensional magnetic materials. Our goal is to identify promising alternatives to Fe_3GeTe_2 and Fe_3GaTe_2 that not only overcome limitations associated with these compounds, but also exhibit theoretically superior magnetic properties. The results of this work can serve as a roadmap for experimental efforts, offering guidance on which Fe_3XY_2 compounds are more likely to be synthesizable and possess the targeted magnetic and structural properties.

II. RESULTS AND DISCUSSION

For HTP exploration of Fe_3XY_2 compounds, a structural symmetry analogous to that of the experimentally synthesized Fe_3GeTe_2 monolayer was adopted as the initial reference. After structural optimizations, two distinct structural types were identified across the studied compounds. As shown schematically in Fig. 1(a), the centrosymmetric Type I structure have space group $P\bar{6}m2$ (No. 187), whereas the non-centrosymmetric Type II structure belongs to space group $P3m1$ (No. 156). In Type I compounds, similar to Fe_3GeTe_2 and Fe_3GaTe_2 , the Fe_2 sublattice and the X atoms lie within the same horizontal plane. In contrast, Type II compounds exhibit a vertical displacement between the Fe_2 and X atoms, denoted by d , indicating a break in mirror symmetry along the out-of-plane direction. Fig. 1(b) presents the periodic table, highlighting in green the p -block elements considered for the X and Y sites in the Fe_3XY_2 compounds. Based on all possible combinations, a total of 529 unique Fe_3XY_2 compositions were generated and systematically investigated. Fig. 1(c) illustrates the flowchart outlining the high-throughput screening procedure used to identify stable compounds. Following structural optimization, the magnetic ground state of each Fe_3XY_2 composition was determined. While several non-magnetic and ferrimagnetic configurations were identified, none were found to be stable. All compounds that passed the stability criteria exhibit a ferromagnetic (FM) ground state. Fig. 1(d) summarizes the screening results. Out of the initial 529 Fe_3XY_2 compounds, 132 were found to be energetically stable based on cohesive and formation energy analysis. Among these, 38 passed the dynamical stability check via phonon calculations. Two compounds failed to meet the mechanical stability criteria. Subsequent *ab initio* molecular dynamics (AIMD) simulations were performed to assess thermal stability, ultimately identifying 31 compounds that satisfy all four stability criteria. A summary of the structural and magnetic properties of the 31 stable Fe_3XY_2 compounds, along with their chemical formulas, is provided in Table I. Fig. 1(e) highlights the elements occupying the X and Y sites in the stable compounds, marked in pink and gold, respectively. It can be noted that the X site is never occupied by halogen elements, whereas the Y site is typically occupied by heavier elements from the pnictogen, chalcogen, and halogen groups. Details of the stability assessments, including phonon spectra (Fig. S1) and AIMD energy profiles (Fig. S2), are provided in the Supplemental Materials. The cohesive and formation energies are summarized in Table I. A positive cohesive energy indicates that the atoms prefer to bind together, while a negative formation energy implies that the Fe_3XY_2 compounds are energetically more favorable than their constituent bulk counterparts in their elemental form. The elastic constants C_{11} , C_{12} , and C_{66} are also presented in Table I. All listed compounds satisfy the Born–Huang^{25,26} mechanical stability criteria for hexagonal monolayers (i.e. $C_{11} > |C_{12}|$ and $C_{66} > 0$)²⁷.

Extracted spin and orbital moments for Fe_1 and Fe_2 sublattices are also listed in Table I (Fe_3 sublattice is symmetrically equivalent to Fe_1 in centrosymmetric systems). Fig. 2(a) and (b) show scatter plots of the spin and orbital magnetic mo-

ments vs. the unit cell volume, respectively. In general, both spin and orbital moments tend to increase with increasing cell volume. In general, Fe atoms tend to exhibit higher magnetic moments as the atomic volume per Fe increases, even in elemental bulk forms. This behavior is primarily attributed to the reduced bandwidth resulting from increased interatomic spacing, which enhances the localization of d -electrons²⁸. The green-shaded region in Fig. 2(a) highlights the compounds exhibiting the highest average spin magnetic moments per Fe atom. Notably, all these compounds are halides, with Fe_3SeI_2 and Fe_3SBr_2 showing average spin moments of approximately $3.0 \mu_B$, significantly higher than that of Fe_3GeTe_2 ($2.23 \mu_B$). A mixed valence state between +2 and +3 is expected for Fe_3GeTe_2 ²⁹. In this range, Fe atoms possess three to four unpaired electrons, corresponding to a spin-only magnetic moment of approximately $3.9\text{--}4.9 \mu_B$, as given by the relation $\mu_{\text{spin-only}} = \sqrt{n(n+2)} \mu_B$. Element-specific X-ray magnetic circular dichroism (XMCD) measurements by K. Yamagami *et al.*^{30,31} revealed that the reduced magnetic moment arises from strong hybridization between Fe $3d$ orbitals and the p orbitals of neighboring Te and Ge atoms. This hybridization leads to significant band broadening and delocalization of Fe d -electrons. Our recent study on 2D metallic magnets FeXZ_2 ($X = \text{Nb, Ta}$; $Z = \text{S, Se, Te}$) reveals that hybridization between Fe d -orbitals and chalcogen p -orbitals plays a key role in governing the magnetic properties³². Accordingly, the hybridization between Fe and halogen atoms in halide-containing compounds is expected to be weaker compared to chalcogen counterparts. Considering that Br has a smaller atomic radius than Te, the larger unit cell volume observed in halides such as Fe_3GaBr_2 compared to Fe_3GaTe_2 can be attributed to the weaker hybridization between Fe and Br atoms. This reduced hybridization results in less bonding contraction, thereby allowing for a more expanded lattice. Moreover, it can be observed that compounds with P occupying the X site exhibit the smallest average magnetic moments (see the yellow highlighted zone). This trend can be attributed to the significant hybridization between the p -orbitals of P atoms and the d -orbitals of Fe atoms, which leads to a reduction in the localized magnetic moment on Fe. The orbital moment scatter plot in Fig. 2(b) reveals that the orbital moments depend not only on structural parameters but also on the spin–orbit coupling (SOC) strength of the X and Y elements. Among the studied compounds, Fe_3PBi_2 exhibits the highest average orbital moment per Fe atom, whereas systems containing lighter elements, such as Fe_3BS_2 , show a low orbital moment.

Fig. 2(c) presents the magnetic anisotropy energy (MAE) of the stable compounds in ascending order. A negative MAE indicates easy-plane magnetism, whereas a positive value corresponds to perpendicular (out-of-plane) easy-axis magnetism. The calculated MAE values for Fe_3GeTe_2 and Fe_3GaTe_2 are in excellent agreement with previously reported results^{33,34}. Notably, Fe_3SiTe_2 exhibits a larger perpendicular MAE compared to Fe_3GeTe_2 , suggesting enhanced magnetic anisotropy in this compound. While the strong SOC of Te atoms is an important contributor, the enhanced MAE observed in the presence of Si suggests that magnetic anisotropy is further influenced by electronic factors, particularly p – d orbital hybridiza-

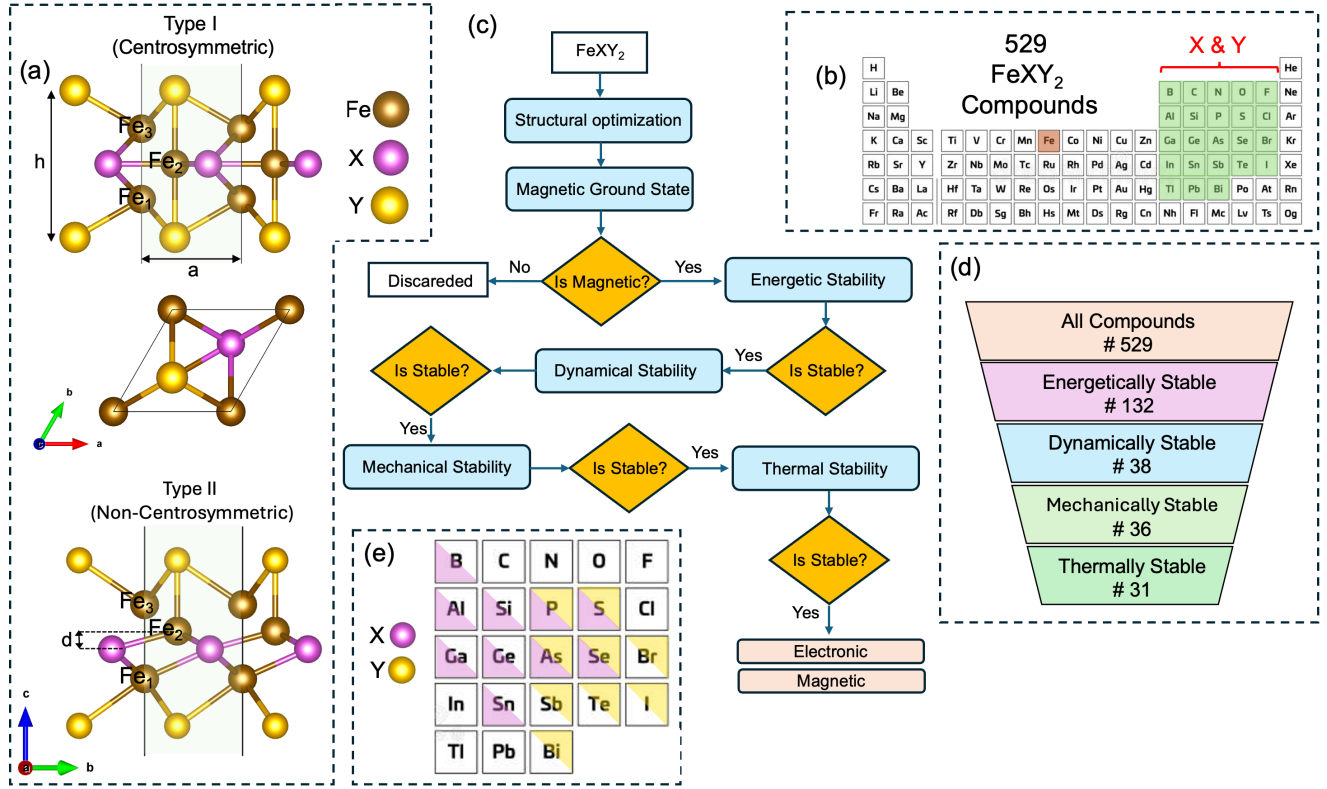


FIG. 1. (a) Structural configuration of the Fe_3XY_2 monolayers depicted from both top and side views. Type I and Type II structures correspond to centrosymmetric and non-centrosymmetric ground states, respectively. The light-green shaded region highlights the unit cell, where a denote the lattice parameter, h represents the thickness. (b) Periodic table highlighting in green the elements that can occupy the X and Y sites, yielding 529 possible compounds. (c) Flowchart of high-throughput identification of stable compounds. (d) Schematic showing the number of stable compounds remaining after successive stability criteria checks, yielding 31 stable compounds. (e) p -block of the periodic table, with X-site elements of stable compounds highlighted in pink and Y-site elements of stable compounds highlighted in gold.

tion.

Fig. 2(d) shows the atom-resolved MAE for three representative cases: Fe_3SiTe_2 , which exhibits the strongest MAE among the studied compounds, synthesized Fe_3GeTe_2 , and the non-centrosymmetric system Fe_3AsBr_2 . Atom-resolved MAE data for all other compounds are provided in the supplementary materials (see `atom-resolved-mae.txt` in each corresponding folder). It can be observed that, in general, Fe_3SiTe_2 and Fe_3GeTe_2 exhibit similar atom-resolved MAE profiles, except for the direction of MAE in the Fe_2 sublattice. This difference can be attributed to the variation in hybridization between the Fe_2 atoms and the X-site elements. Specifically, the hybridization between Fe_2 and Si promotes perpendicular anisotropy, whereas the interaction between Fe_2 and Ge favors in-plane MAE. This distinction explains the overall enhancement of perpendicular anisotropy in Fe_3SiTe_2 . Moreover, in the non-centrosymmetric Fe_3AsBr_2 , an asymmetric distribution of atom-resolved MAE is observed: the Fe_1 , Fe_2 , and Br_{Dn} sublayers exhibit positive MAE values, whereas Fe_3 and Br_{Up} show negative contributions. The competition among these opposing anisotropies leads to an overall reduction in the total MAE of the compound. In later sections, it will be shown that this reduction in MAE plays a crucial role

in stabilizing skyrmions in this compound. Fig. 2(e) presents the strength of the D_{11} (Dzyaloshinskii–Moriya interaction, DMI) across all dynamically stable compounds. Te-based systems generally exhibit strong D_{11} values, with Fe_3AlTe_2 showing the highest at 5.71 meV. In contrast, halide compounds show relatively weak DMI; for example, Fe_3GaI_2 has $D_{11} = 0.97$ meV. It can be inferred that, similar to MAE, the strength of the DMI is not solely determined by the SOC strength of the constituent elements. Instead, the hybridization between atomic orbitals also plays a significant role in governing the magnitude of DMI. It should be mentioned that in centrosymmetric systems, the DMI vectors cancel due to symmetry, regardless of their individual magnitudes, and therefore chiral spin textures are not expected in these compounds.

The Heisenberg exchange interactions (J_{ij}) were extracted for all Fe_3XY_2 compounds, and a summary of the results is presented in Fig. 3(a–d). The complete datasets of J_{ij} and D_{ij} as functions of interatomic distance are available in the Supplemental Materials, in corresponding folder for each compound. Fig. 3(a) displays the strength of the J_{13} exchange interaction, sorted in ascending order for all Fe_3XY_2 compounds. In general, J_{13} is found to be strong, reaching up to

TABLE I. The optimized lattice constant a (Å); thickness c (Å); symmetry (Cen.: centrosymmetric, Non. : non-centrosymmetric); pair distances d_{13} (Fe₁–Fe₃, Å) and d_{12} (Fe₁–Fe₂, Å); cohesive energy E_{coh} (eV/atom); formation energy E_f (meV/atom); elastic constants C_{ij} (GPa); spin magnetic moment per Fe atom $M_{\text{Fe}}^{\text{spin}}$ (μ_B); orbital magnetic moment per Fe atom $M_{\text{Fe}}^{\text{orb}}$ (μ_B); exchange parameters J_{ij} (meV); exchange stiffness A (meV.Å²); spiralization constant D (meV.Å); magnetic anisotropy energy (MAE, meV/f.u.); and Curie temperature T_c (K) for Fe_3XY_2 monolayers.

Struct.	a (Å)	c (Å)	Sym.	d_{13} (Å)	d_{12} (Å)	E_{coh} (eV/atom)	E_f (eV/atom)	C_{11} (GPa)	C_{12} (GPa)	C_{66} (GPa)	$M_{\text{Fe}_1}^{\text{spin}}$ (μ_B)	$M_{\text{Fe}_2}^{\text{spin}}$ (μ_B)	$M_{\text{Fe}_1}^{\text{orb}}$ (μ_B)	$M_{\text{Fe}_2}^{\text{orb}}$ (μ_B)	J_{13} (meV)	J_{12} (meV)	J_{22} (meV)	A (meV.Å ²)	D (meV.Å)	MAE (meV/f.u.)	T_c (K)
Fe ₃ P ₃	3.71	4.61	Cen.	2.80	2.56	5.28	-0.16	741.49	578.76	81.37	2.21	0.36	0.034	-0.007	58.21	6.17	-2.10	292.28	0.00	0.26	247
Fe ₃ PA ₂	3.77	4.88	Cen.	2.64	2.55	5.04	-0.15	653.54	537.13	58.21	2.34	0.60	0.031	0.002	59.21	11.89	-1.86	558.91	0.00	0.04	671
Fe ₃ PSb ₂	3.84	5.32	Cen.	2.49	2.55	4.81	-0.09	623.39	525.81	48.79	2.32	0.92	0.038	0.001	64.07	16.51	-3.74	531.87	0.00	-0.87	579
Fe ₃ PBi ₂	3.87	5.60	Cen.	2.44	2.54	4.65	-0.04	527.35	455.40	35.98	2.41	1.26	0.071	-0.004	67.38	22.26	-5.89	565.85	0.00	1.23	610
Fe ₃ BS ₂	3.59	4.48	Cen.	2.52	2.43	5.17	-0.23	658.06	469.16	94.45	2.37	0.92	0.020	0.013	55.15	9.58	-2.89	432.52	0.00	-0.34	606
Fe ₃ GeS ₂	3.95	4.38	Cen.	2.57	3.95	4.51	-0.20	636.94	309.01	163.96	2.75	0.45	0.028	0.012	56.10	7.36	-0.98	473.82	0.00	-0.37	605
Fe ₃ SiS ₂	3.85	4.47	Cen.	2.60	2.57	5.00	-0.27	727.60	446.59	140.51	2.74	0.89	0.027	0.011	91.25	15.99	-8.11	314.65	0.00	-0.08	255
Fe ₃ GeS ₂	3.93	4.48	Cen.	2.66	2.63	4.74	-0.17	696.00	409.75	143.13	2.85	0.89	0.027	0.015	99.19	15.87	-4.06	446.98	0.00	-0.44	410
Fe ₃ AsS ₂	3.93	4.56	Non.	2.76	2.62	4.74	-0.14	574.01	420.05	76.72	2.87	1.14	0.030	0.015	75.48	25.76	-11.20	376.98	0.59	-0.07	301
Fe ₃ BSe ₂	3.65	4.81	Cen.	2.43	2.43	4.90	-0.17	581.49	435.22	73.13	2.39	1.19	0.025	0.011	71.43	21.97	-2.60	516.21	0.00	0.33	721
Fe ₃ AlSe ₂	4.00	4.65	Cen.	2.46	2.62	4.46	-0.23	631.09	290.53	170.28	2.64	0.91	0.034	0.014	57.11	10.89	-0.73	519.55	0.00	0.27	629
Fe ₃ GaSe ₂	4.01	4.67	Cen.	2.48	2.62	4.31	-0.21	637.31	294.73	171.29	2.68	0.85	0.036	0.014	52.32	10.37	-1.58	482.27	0.00	0.83	595
Fe ₃ SiSe ₂	3.91	4.76	Cen.	2.50	2.58	4.79	-0.28	681.80	430.39	125.71	2.68	1.08	0.030	0.010	90.82	21.49	-8.15	410.02	0.00	0.93	446
Fe ₃ GeSe ₂	3.99	4.77	Cen.	2.55	2.64	4.54	-0.19	644.09	391.26	126.42	2.77	1.13	0.034	0.016	100.66	22.99	-4.88	530.27	0.00	0.47	551
Fe ₃ SnSe ₂	4.20	4.75	Cen.	2.60	2.75	4.27	-0.02	549.05	360.01	94.52	2.85	1.32	0.036	0.032	94.03	20.39	-5.66	553.24	0.00	-0.55	543
Fe ₃ BTe ₂	3.69	5.34	Cen.	2.38	2.44	4.65	-0.04	329.63	139.34	95.14	2.29	1.64	0.033	0.011	100.62	28.01	-4.68	372.35	0.00	3.28	457
Fe ₃ AlTe ₂	4.07	5.04	Cen.	2.40	2.64	4.29	-0.18	625.56	288.70	168.43	2.52	1.42	0.044	0.017	77.16	22.01	-0.58	630.81	0.00	0.83	772
Fe ₃ GaTe ₂	4.07	5.06	Cen.	2.42	2.64	4.14	-0.16	626.39	277.36	174.51	2.54	1.41	0.044	0.022	85.10	22.32	-1.05	609.97	0.00	0.55	667
Fe ₃ SiTe ₂	3.97	5.14	Cen.	2.43	2.59	4.61	-0.21	633.35	377.17	128.09	2.52	1.36	0.037	0.013	93.53	31.65	-11.49	395.85	0.00	5.03	453
Fe ₃ GeTe ₂	4.05	5.14	Cen.	2.47	2.65	4.37	-0.13	609.45	356.01	126.72	2.63	1.46	0.042	0.022	87.82	30.43	-5.64	545.60	0.00	4.15	611
Fe ₃ SnTe ₂	4.26	5.10	Cen.	2.52	2.76	4.13	0.00	547.25	321.94	112.66	2.73	1.47	0.045	0.036	96.46	27.79	-4.42	616.69	0.00	1.63	619
Fe ₃ PTe ₂	3.76	5.55	Non.	2.45	2.45	4.61	-0.22	588.83	329.14	129.85	2.56	1.31	0.038	0.008	43.92	43.92	-6.30	174.58	8.58	1.21	272
Fe ₃ AlBr ₂	4.07	5.22	Cen.	2.33	2.62	3.75	-0.14	476.35	208.76	133.80	2.79	2.06	0.036	0.027	86.68	44.04	-2.44	794.61	0.00	-0.33	906
Fe ₃ GaBr ₂	4.08	5.24	Cen.	2.34	2.63	3.63	-0.15	462.42	199.73	131.34	2.87	2.13	0.037	0.036	95.05	40.97	-3.91	763.88	0.00	-0.28	852
Fe ₃ AsBr ₂	3.92	5.72	Non.	2.44	2.44	3.88	-0.12	439.32	257.12	91.10	2.70	1.61	0.048	0.018	53.81	53.74	-16.76	327.54	9.31	0.53	447
Fe ₃ SBr ₂	3.99	5.46	Cen.	2.51	2.62	3.89	-0.21	333.81	257.41	38.20	3.24	2.53	0.031	0.019	77.56	51.04	-10.15	334.88	0.00	-0.44	231
Fe ₃ AlI ₂	4.12	5.48	Cen.	2.33	2.65	3.66	-0.10	520.62	215.36	152.63	2.73	2.09	0.036	0.032	94.77	45.31	-2.16	809.70	0.00	-0.77	891
Fe ₃ GaI ₂	4.12	5.49	Cen.	2.34	2.65	3.52	-0.10	499.19	183.75	157.72	2.82	2.09	0.036	0.040	110.56	43.49	-3.30	826.10	0.00	1.16	914
Fe ₃ SiI ₂	3.99	5.74	Cen.	2.37	2.59	3.95	-0.11	526.16	236.53	144.81	2.66	2.04	0.042	0.031	61.26	36.51	-15.70	522.02	0.00	0.74	605
Fe ₃ GeI ₂	4.10	5.67	Cen.	2.38	2.65	3.73	-0.05	446.80	182.93	131.93	2.72	2.12	0.049	0.031	76.67	34.47	-4.30	774.62	0.00	1.08	888
Fe ₃ SI ₂	4.06	5.79	Cen.	2.48	2.65	3.71	-0.09	325.92	270.46	27.73	3.18	2.58	0.031	0.022	104.41	51.52	-8.83	416.89	0.00	0.02	165
Fe ₃ SeI ₂	4.20	5.77	Cen.	2.50	2.72	3.54	-0.02	349.74	249.66	50.04	3.18	2.64	0.034	0.029	84.33	48.34	-7.52	387.53	0.00	0.43	160
Fe ₃ AsI ₂	3.99	5.96	Non.	2.48	2.48	3.74	-0.03	452.00	232.96	109.52	2.53	1.74	0.035	0.025	56.87	56.68	-13.03	181.55	4.71	-0.66	307

110 meV in Fe₃GaI₂. This strong interaction is recognized as the primary contributor to the elevated T_c in Fe₃GeTe₂³³. Fig. 3(b) and (c) show the values of J_{12} and J_{22} interactions, respectively. While both J_{13} and J_{12} consistently exhibit FM character, J_{22} is AFM in all compounds. This behavior aligns with prior findings that intra-sublayer interactions are inherently AFM in Fe₃GeTe₂³³.

Although J_{12} and J_{22} often follow similar trends (e.g., both are strong in Fe₃AsBr₂ and Fe₃AsI₂), their behavior does not correlate with that of J_{13} . To further investigate potential correlations, a heatmap of Pearson correlation coefficients between exchange interactions and interatomic distances is presented in Fig. 3(e). Coefficients near +1 or −1 indicate strong direct or inverse correlations, respectively. Statistical significance is denoted by asterisks: * for $p < 0.1$, ** for $p < 0.05$, and *** for $p < 0.01$.

The heatmap reveals a strong correlation between J_{12} and J_{22} , with high statistical significance. The inverse correlation arises from the fact that J_{22} is consistently antiferromagnetic (AFM) and thus carries a negative sign. In contrast, J_{13} shows

no meaningful correlation with either J_{12} or J_{22} , nor with any of the pair distances, including d_{13} . Interestingly, J_{12} exhibits a significant inverse correlation with d_{13} , while both J_{12} and J_{22} show strong correlations with d_{22} . These results suggest that while J_{12} and J_{22} are governed by geometric factors such as atomic separations, the dominant J_{13} interaction follows a different, less distance-dependent mechanism.

To gain insight into the origin of the observed exchange interactions and their peculiar correlations, we analyzed the orbital-resolved contributions to J_{13} (Fig. 3(f)), J_{12} (Fig. 3(g)), and J_{22} (Fig. 3(h)), where the dominant orbital channels are highlighted in orange. It is evident that the d_{z^2} – d_{z^2} channel dominates the J_{13} exchange interaction. Fig. 3(i) schematically illustrates the spatial alignment of the d_{z^2} orbitals on Fe₁ and Fe₃ atoms, which are vertically aligned, along with the adjacent p_z orbital of the Ge atom. The double-headed orange arrows and associated values indicate the tight-binding hopping parameters between the shown orbitals. Due to this vertical alignment, a direct overlap between the d_{z^2} orbitals of Fe₁ and Fe₃ is expected and confirmed by a strong hop-

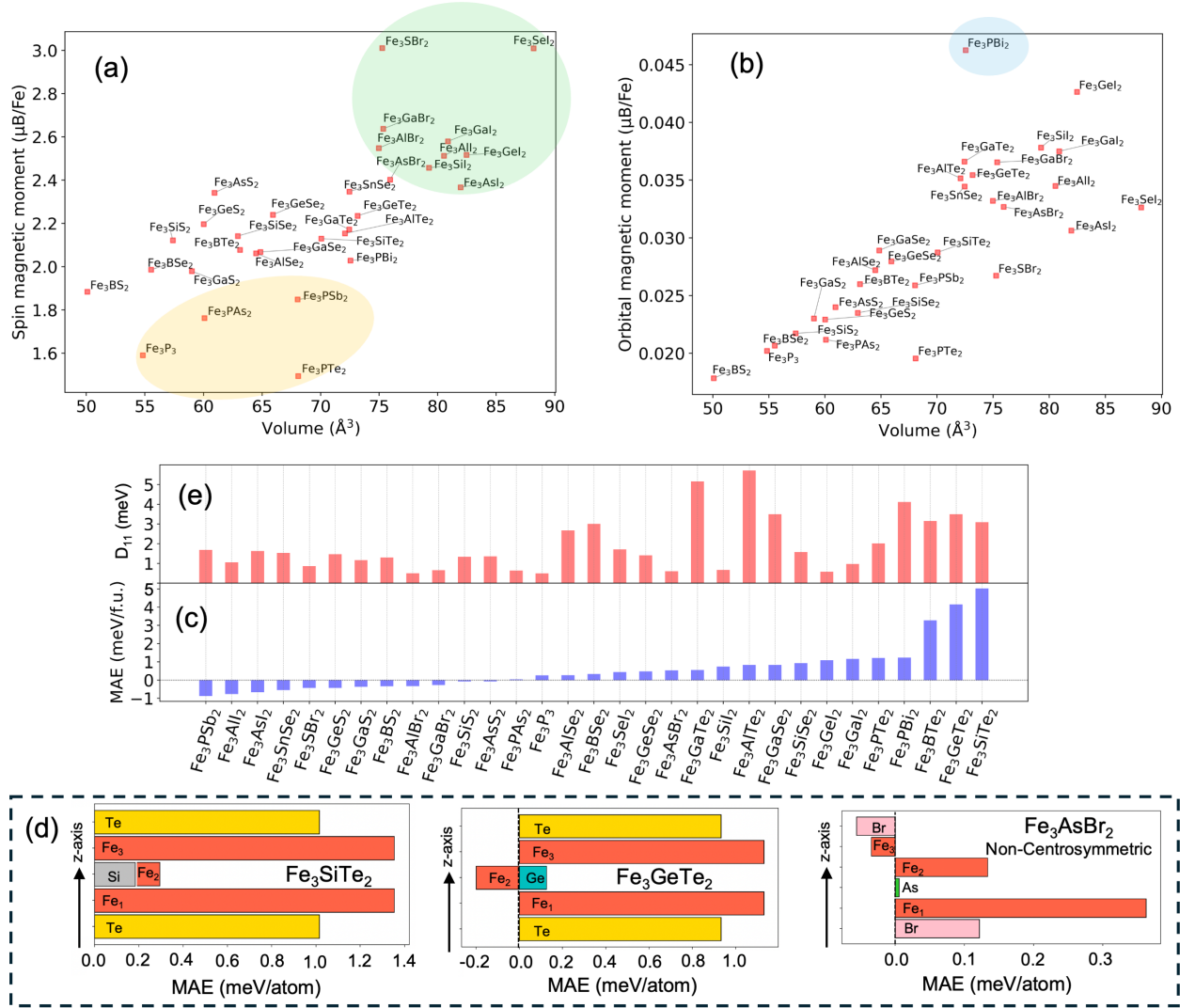


FIG. 2. (a) Scatter plot of the averaged spin magnetic moment per Fe vs. cell volume, where the green zone highlights halides with the highest averaged moments and the yellow zone highlights compounds containing P at the X site with the lowest magnetic moments. (b) Scatter plot of the averaged orbital magnetic moment per Fe vs. cell volume, where the highest orbital moment is highlighted in blue. (c) Magnetic anisotropy energy (MAE) sorted in ascending order for 31 stable compounds. (d) Corresponding D_{11} values. (e) Atom-resolved MAE for Fe₃SiTe₂ (the compound with the strongest MAE), Fe₃GeTe₂ (the synthesized monolayer) and Fe₃AsBr₂ (a non-centrosymmetric compound).

ping parameter of $t = 0.7$ eV. Additionally, the p_z orbital of the Ge atom mediates an indirect interaction between the d_{z^2} orbitals of Fe₁ and Fe₃, supported by a relatively strong hopping parameter of $t = 0.4$ eV. These findings suggest that J_{13} is primarily governed by a direct exchange mechanism, while indirect exchange via the p -orbitals of the Ge atom also has a contribution.

A similar analysis was performed for J_{12} , where the dominant exchange channel is found to be between d_{z^2} - d_{xz} orbitals, as shown in Fig. 3(j). In this case, a direct overlap between the d -orbitals of Fe atoms is spatially less probable, which is reflected in the very weak direct hopping parameter of $t = 0.03$ eV. However, the p -orbital of the neighboring Ge atom mediates an indirect exchange between the d -orbitals

with a relatively strong hopping parameter of $t = 0.6$ eV. This indicates that J_{12} is predominantly governed by an indirect exchange mechanism facilitated by p - d hybridization. In the same manner, for the AFM J_{22} interaction, the dominant exchange channel is also between d_{z^2} - d_{z^2} orbitals, as shown in Fig. 3(h). However, since the two Fe atoms involved in this interaction lie in the same xy -plane, a direct orbital overlap is not feasible. Therefore, the exchange interaction is expected to be mediated indirectly through the p -orbitals of neighboring Ge and Te atoms.

These findings suggest that J_{13} is less sensitive to structural parameters and uncorrelated with J_{12} or J_{22} due to its primarily direct exchange mechanism. In contrast, both J_{12} and J_{22} exhibit strong mutual correlation and dependence on struc-

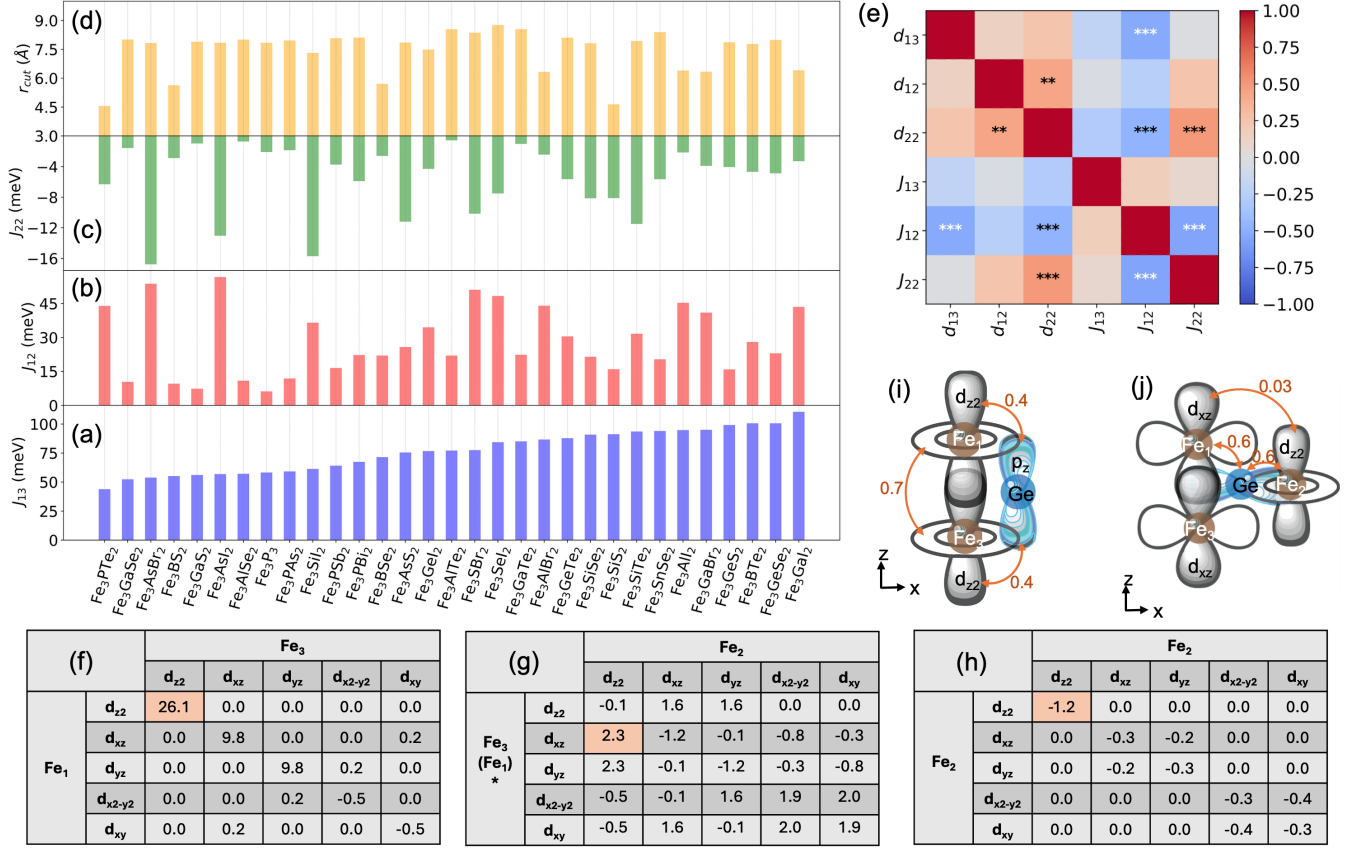


FIG. 3. Analysis of Heisenberg exchange interactions. (a) J_{13} , sorted in ascending order for 31 stable compounds. (b) J_{12} (c) J_{22} , negative sign indicates AFM nature of interaction, (d) the cut off radius where strength of exchange interactions drops below 1 meV. (e) Heatmap of Pearson correlation coefficients between pair distances and exchange interactions. Each box displays the correlation coefficient, with values close to +1 or -1 indicating strong direct or inverse relationships, respectively. Asterisks denote the statistical significance of each correlation: * for $p < 0.1$, ** for $p < 0.05$, and *** for $p < 0.01$. (f–h) Orbital-decomposed exchange interactions for J_{13} (f), J_{12} (g), and J_{22} (h), with the strongest interaction highlighted in orange. Positive and negative values correspond to FM and AFM interactions, respectively. (i) and (j) Schematic illustration of the p - and d -orbitals involved in the strongest interactions for J_{13} and J_{12} , respectively. The orange double-headed arrows and the number next to them represent the Wannierization hopping parameters between orbitals, given in meV.

tural features, consistent with their shared indirect exchange nature mediated by the p -orbitals of the X and Y atoms.

Figure 3(d) presents the cutoff radius beyond which the strength of exchange interactions falls below 1 meV. For most compounds, this cutoff lies in the range of 7–8 Å, indicative of long-range magnetic interactions typically observed in metallic systems. Interestingly, despite all compounds exhibiting metallic character (as confirmed by the electronic band structures in Fig. S3), certain materials such as Fe_3PTe_2 and Fe_3SiS_2 show significantly shorter interaction ranges, with cutoff radii as low as 4.5 Å.

Fig. 4(a) presents a scatter plot of the magnetic transition temperatures (T_c), estimated via Monte Carlo simulations, versus the exchange stiffness (A). As expected, a general linear trend is observed, where higher exchange stiffness correlates with increased T_c . Notably, halide compounds (highlighted in green) exhibit higher T_c values than those of the experimentally synthesized Fe_3GeTe_2 and Fe_3GaTe_2 . This suggests that synthesizing Fe_3XY_2 compounds with halogens

at the Y site may lead to new 2D ferromagnets with record-high transition temperatures, enabling room-temperature spintronic applications.

It is important to note that Monte Carlo simulations based on GGA-extracted exchange parameters tend to overestimate T_c due to the known overestimation of exchange interactions within GGA. This limitation can be addressed by incorporating dynamical electronic correlations via DMFT, although DMFT is computationally prohibitive for high-throughput studies. Prior studies on the Fe_nGeTe_2 family show that the primary correction from DMFT is a renormalization of J_{13} by approximately a factor of two, attributed to the correlation-induced broadening of Fe d_{z^2} orbitals³³.

The two insets in Fig. 4(a) depict the spin textures at $T = 0$ K for Fe_3GaI_2 (with the highest T_c) and Fe_3SeI_2 (with the lowest T_c) among the stable compounds. Fe_3GaI_2 exhibits a fully collinear ferromagnetic configuration, consistent with its strong ferromagnetic exchange interactions (e.g., $J_{13} = 110.6$ meV and $J_{12} = 43.5$ meV) and relatively weak

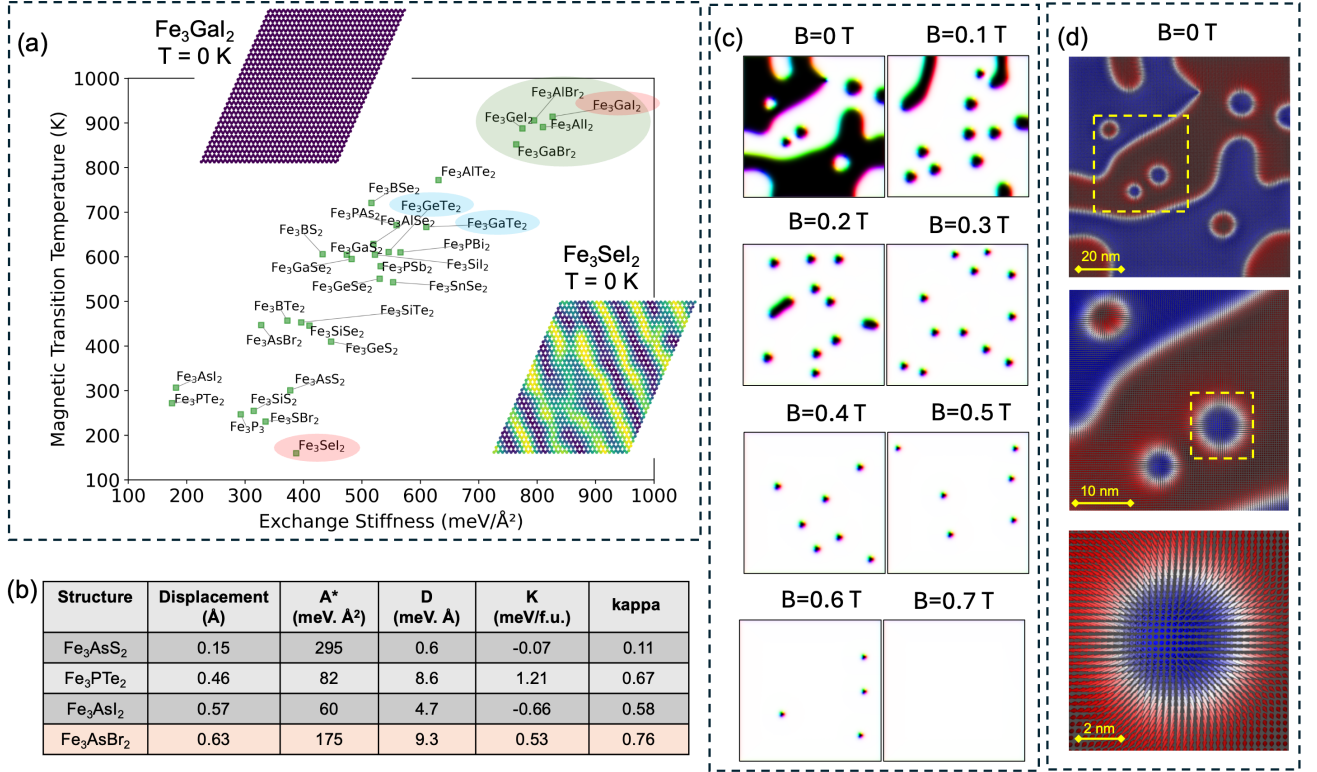


FIG. 4. (a) Scatter plot of the magnetic transition temperature (T_c) vs. exchange stiffness (A), where the two synthesized compounds Fe₃GeTe₂ and Fe₃GaTe₂ are highlighted in blue. The green zone highlights halide compounds, which exhibit the highest magnetic transition temperatures, while the compounds with the highest (T_c for Fe₃GaI₂) and lowest (T_c for Fe₃SeI₂) values are highlighted in red. Two insets show the Monte Carlo spin texture at $T = 0$ K for Fe₃GaI₂ and Fe₃SeI₂, where dark blue represents up-spin alignment and yellow represents down-spin alignment. Fe₃GaI₂ exhibits a collinear spin texture, whereas Fe₃SeI₂ shows spin spirals. (b) List of non-centrosymmetric compounds, ordered based on centrosymmetry-breaking displacements between Fe₂ and X, together with the corresponding micromagnetic quantities: exchange stiffness (A), spiralization constant (D), and magnetic anisotropy (K). The only combination that exhibits a topological spin texture is highlighted in orange. (c) Micromagnetic simulation for Fe₃AsBr₂ as a function of external magnetic field, where skyrmions emerge at $B = 0$ T, shrink in size with increasing magnetic field, and vanish for fields larger than $B = 0.7$ T. (d) Colored zero-field ($B = 0$ T) spin texture of Fe₃AsBr₂, with the middle and bottom panels zoomed into the Néel-type skyrmionic texture. Red indicates spin-up alignment, while blue indicates spin-down alignment.

antiferromagnetic interactions ($J_{22} = -3.3$ meV). In contrast, Fe₃SeI₂ exhibits non-collinear spin spirals at $T = 0$ K, arising from competing ferromagnetic and antiferromagnetic interactions. This frustration leads to a lower thermal stability of magnetic order and consequently a reduced T_c .

In Fig. 4(b), systems with non-centrosymmetric structural ground states are shown, sorted by the vertical displacement between Fe₂ and X atoms. The exchange stiffness (A) and the spiralization tensor (\mathbf{D}) were computed using the following expressions³⁵:

$$A = \frac{1}{2} \sum_{j \neq i} J_{ij} R_{ij}^2 e^{-\mu R_{ij}}, \quad (1)$$

$$D_{\alpha\beta} = \sum_{j \neq i} D_{ij}^{\alpha} R_{ij}^{\beta} e^{-\mu R_{ij}}, \quad (2)$$

where J_{ij} and D_{ij}^{α} represent the isotropic and DMI exchange interactions between atomic sites i and j , respectively, and R_{ij}

denotes the distance between them. The exponential damping factor $e^{-\mu R_{ij}}$ ensures convergence with respect to the real-space cutoff. To accurately determine A and \mathbf{D} , the parameter μ was varied between 2 and 4, and the results were extrapolated to $\mu = 0$ using a third-order polynomial fit^{36,37}. In two-dimensional systems, the interfacial Dzyaloshinskii–Moriya interaction (DMI) typically dominates, leading to a characteristic form of the spiralization matrix. As a result, the spiralization tensor generally takes the form:

$$\mathbf{D} = \begin{bmatrix} 0 & D & 0 \\ -D & 0 & 0 \\ 0 & 0 & 0 \end{bmatrix},$$

where D denotes the scalar spiralization constant, expressed in units of meV·Å. For each compound, the normalized exchange stiffness (A^* , where J_{13} is halved), spiralization constant (D), and magnetic anisotropy energy (K) are listed, as key input parameters for micromagnetic simulations. To

quantify the competition between these parameters, a dimensionless stability criterion κ is commonly used to assess the likelihood of chiral magnetic states³⁸, defined as:

$$\kappa = \frac{\pi D}{4\sqrt{AK}}. \quad (3)$$

In general, $\kappa > 1$ (or close to 1) is considered favorable for stabilizing skyrmions. The calculated κ values for each system are listed in the last column. Micromagnetic simulations showed trivial spin textures for all compounds except Fe_3AsBr_2 , which is highlighted in orange.

Fig. 4(c) illustrates the evolution of the spin texture in Fe_3AsBr_2 under varying external magnetic fields. Notably, skyrmion-like spin textures are present even at zero external field ($B = 0$ T). As the magnetic field increases, the skyrmions shrink and eventually vanish at fields above $B = 0.7$ T. Fig. 4(d) presents a magnified view of the spin texture at $B = 0$ T, with two zoomed-in regions (highlighted by dashed yellow boxes) shown in the lower panels. The observed spin texture is consistent with Néel-type skyrmions, with a characteristic diameter of approximately 10 nm.

To confirm the topological nature of these spin textures, the winding number was computed using:

$$N_{\text{sk}} = \frac{1}{4\pi} \int \mathbf{m} \cdot \left(\frac{\partial \mathbf{m}}{\partial x} \times \frac{\partial \mathbf{m}}{\partial y} \right) dx dy. \quad (4)$$

The result yields a winding number close to $N_{\text{sk}} = 1$ ³⁹, verifying the topologically non-trivial nature of the magnetic configuration and confirming the presence of Néel-type skyrmions.

III. METHODOLOGY

First-principles structural optimization, stability analysis, and calculation of magnetic ground state were conducted in the framework of density functional theory (DFT)^{40,41} using the Vienna *Ab initio* Simulation Package (VASP)^{42–45}. The exchange-correlation potential was treated using the generalized gradient approximation (GGA) functional in conjunction with the Perdew, Burke, and Ernzerhof (PBE) method⁴⁶. The projector augmented wave method⁴⁷ was applied. A plane-wave basis set with a kinetic cutoff energy of 500 eV was used to expand the electronic wave function, and a vacuum space of at least 20 Å was inserted along *c*-axis to prevent unrealistic interactions between periodic images. During structural optimization, the maximum force on each atom was less than 5×10^{-3} eV/Å. A Gaussian smearing factor of 0.05 was taken into account. Brillouin zone (BZ) integration was performed by a Γ -centered $9 \times 9 \times 1$ uniform *k*-point grid for monolayers. To ensure the dynamical stability of the systems, the phonon dispersions were calculated, using the finite-displacement approach, implemented in the PHONOPY⁴⁸ package. To analyze the thermal stability, *ab initio* molecular dynamics (AIMD) simulations were conducted, using a microcanonical ensemble (NVE), at constant temperatures of $T = 500$ K for a simulation period of 5 ps with 1 fs time steps. A $3 \times 3 \times 1$ supercell was used for phonon dispersions and

AIMD. For the calculation of Heisenberg exchange interactions (J_{ij} and D_{ij}) and magnetic anisotropy energy (MAE), a $25 \times 25 \times 1$ *k*-point grid was utilized, and the spin-orbit coupling (SOC) was taken into account. All magnetic properties (Magnetic moments, Heisenberg exchange interaction, DMI, MAE, and atom resolved MAE) were calculated via the QuantumATK-Synopsys package version U-2022, employing an LCAO basis set, the "PseudoDojo" pseudopotential^{49,50}, a density mesh cutoff of 120 Hartree. The projection into localized Wannier Functions (WFs) was carried out using the Wannier90 package⁵¹, via VASP to Wannier90 interface. The WFs basis set comprised five d-orbitals of transition metal and three p-orbitals of X and Y atoms. The tight-binding hopping parameters were extracted from WFs. The TB2J⁵² package was utilized to calculate orbital resolved isotropic exchange interactions via Liechtenstein, Katsnelson, Antropov, and Gubanov (LKAG)⁵³ formalism. The extracted exchange interactions and MAE were implemented in a Heisenberg Hamiltonian to calculate the magnetic ordering temperature by performing classical Monte Carlo (MC) simulations via UppASD code⁵⁴. To achieve properly averaged properties, five ensembles within a supercell of $32 \times 32 \times 1$ were modeled, assuming periodic boundary conditions. Micromagnetic simulations were performed using MuMax3^{55,56}. The unit cell dimensions were obtained from relaxed structures in *ab initio* calculations and were used to form a grid of $256 \times 256 \times 1$ cells. The Gilbert damping parameter was set to $\alpha = 0.10$ as proposed in a previous study⁵⁷, and uniaxial anisotropy was applied. The simulation time was 1 ns for each set of parameters, ensuring the system would reach an equilibrium state. The values for exchange stiffness (*A*), DMI (*D*), uniaxial anisotropy constant (K_{u1}), and magnetic moment per unit cell (μ) were taken from *ab initio* calculations and converted into the continuous material parameters used in micromagnetic simulations. The system was subjected to an external magnetic field applied perpendicular to the atomic plane, with field magnitudes ranging from 0 T to 1.0 T in steps of 100 mT.

ACKNOWLEDGMENTS

B.S. acknowledges financial support from Swedish Research Council (grant no. 2022-04309 and grant No. 2018-07082). The computations were enabled by resources provided by the National Academic Infrastructure for Supercomputing in Sweden (NAISS) at UPPMAX (NAISS 2024/5-258) and at NSC and PDC (NAISS 2024/3-40) partially funded by the Swedish Research Council through grant agreement no. 2022-06725. B.S. and S. E. also acknowledge EuroHPC for awarding us access to EU2023D11-039 hosted by Karolína at IT4Innovations, Czech Republic. Artificial intelligence was used to improve the language and readability of this work.

DATA AVAILABILITY STATEMENT

All data for stable compounds are presented in the main manuscript and supplementary materials. Data related to un-

stable compounds are also available from the corresponding author upon reasonable request.

CONFLICT OF INTEREST

The authors declare that they have no conflicts of interest to disclose.

- ¹M. Gibertini, M. Koperski, A. F. Morpurgo, and K. S. Novoselov, *Nature nanotechnology* **14**, 408 (2019).
- ²C. Gong and X. Zhang, *Science* **363**, eaav4450 (2019).
- ³B. Huang, G. Clark, E. Navarro-Moratalla, D. R. Klein, R. Cheng, K. L. Seyler, D. Zhong, E. Schmidgall, M. A. McGuire, D. H. Cobden, W. Yao, D. Xiao, P. Jarillo-Herrero, and X. Xu, *Nature* **546**, 270 (2017).
- ⁴C. Gong, L. Li, Z. Li, H. Ji, A. Stern, Y. Xia, T. Cao, W. Bao, C. Wang, Y. Wang, Z. Q. Qiu, R. J. Cava, S. G. Louie, J. Xia, and X. Zhang, *Nature* **546**, 265 (2017).
- ⁵S. Ershadrad, M. Davoudiniya, N. Machacova, and B. Sanyal, *physica status solidi (b)* **261**, 2300496 (2024).
- ⁶Z. Fei, B. Huang, P. Malinowski, W. Wang, T. Song, J. Sanchez, W. Yao, D. Xiao, X. Zhu, A. F. May, *et al.*, *Nature materials* **17**, 778 (2018).
- ⁷J. Seo, D. Y. Kim, E. S. An, K. Kim, G.-Y. Kim, S.-Y. Hwang, D. W. Kim, B. G. Jang, H. Kim, G. Eom, *et al.*, *Science advances* **6**, eaay8912 (2020).
- ⁸A. F. May, D. Ovchinnikov, Q. Zheng, R. Hermann, S. Calder, B. Huang, Z. Fei, Y. Liu, X. Xu, and M. A. McGuire, *ACS nano* **13**, 4436 (2019).
- ⁹S. Ershadrad, S. Ghosh, D. Wang, Y. Kvashnin, and B. Sanyal, *The Journal of Physical Chemistry Letters* **13**, 4877 (2022).
- ¹⁰C. Tian, F. Pan, S. Xu, K. Ai, T. Xia, and P. Cheng, *Applied Physics Letters* **116** (2020).
- ¹¹S. Ghosh, S. Ershadrad, and B. Sanyal, *2D Materials* **11**, 035002 (2024).
- ¹²B. Zhao, R. Ngaley, S. Ghosh, S. Ershadrad, R. Gupta, K. Ali, A. M. Hoque, B. Karpiak, D. Khokhriakov, C. Polley, *et al.*, *Advanced Materials* **35**, 2209113 (2023).
- ¹³R. Ngaley, B. Zhao, S. Ershadrad, R. Gupta, M. Davoudiniya, L. Bainsla, L. Sjostrom, M. A. Hoque, A. Kalaboukhov, P. Svedlindh, *et al.*, *ACS nano* **18**, 5240 (2024).
- ¹⁴B. Zhao, L. Bainsla, S. Ershadrad, L. Zeng, R. Ngaley, P. Svedlindh, E. Olsson, B. Sanyal, and S. P. Dash, *Advanced Materials*, 2502822 (2025).
- ¹⁵G. Zhang, F. Guo, H. Wu, X. Wen, L. Yang, W. Jin, W. Zhang, and H. Chang, *Nature communications* **13**, 5067 (2022).
- ¹⁶H. K. Gweon, S. Y. Lee, H. Y. Kwon, J. Jeong, H. J. Chang, K.-W. Kim, Z. Q. Qiu, H. Ryu, C. Jang, and J. W. Choi, *Nano letters* **21**, 1672 (2021).
- ¹⁷European Chemical Society, “The periodic table of element scarcity,” <https://www.euchems.eu/euchems-periodic-table/> (2019), accessed: 2025-08-24.
- ¹⁸D. Zagorac, H. Müller, S. Ruehl, J. Zagorac, and S. Rehme, *Applied Crystallography* **52**, 918 (2019).
- ¹⁹A. Jain, S. P. Ong, G. Hautier, W. Chen, W. D. Richards, S. Dacek, S. Cholia, D. Gunter, D. Skinner, G. Ceder, *et al.*, *APL materials* **1** (2013).
- ²⁰S. Hastrup, M. Strange, M. Pandey, T. Deilmann, P. S. Schmidt, N. F. Hinsche, M. N. Gjerding, D. Torelli, P. M. Larsen, A. C. Riis-Jensen, *et al.*, *2D Materials* **5**, 042002 (2018).
- ²¹N. Mounet, M. Gibertini, P. Schwaller, D. Campi, A. Merkys, A. Marrazzo, T. Sohier, I. E. Castelli, A. Cepellotti, G. Pizzi, *et al.*, *Nature nanotechnology* **13**, 246 (2018).
- ²²A. Carlsson, J. Rosen, and M. Dahlqvist, *Computational Materials Science* **239**, 112953 (2024).
- ²³P. Helmer, J. Björk, and J. Rosen, *Inorganic chemistry* **63**, 16645 (2024).
- ²⁴J. Björk, J. Zhou, P. O. Persson, and J. Rosen, *Science* **383**, 1210 (2024).
- ²⁵M. Born and K. Huang, *Dynamical theory of crystal lattices* (Clarendon press, 1954).
- ²⁶F. Mouhat and F.-X. Coudert, *Phys. Rev. B* **90**, 224104 (2014).
- ²⁷M. J. Varjovi, S. Ershadrad, B. Sanyal, and S. Tosoni, *2D Materials* **11**, 015016 (2023).
- ²⁸R. Soulaïrol, C.-C. Fu, and C. Barreteau, *Journal of Physics: Condensed Matter* **22**, 295502 (2010).
- ²⁹D. Backes, R. Fujita, L. Veiga, D. Mayoh, G. Wood, S. Dhesi, G. Balakrishnan, G. van der Laan, and T. Hesjedal, *Nanotechnology* **35**, 395709 (2024).
- ³⁰K. Yamagami, Y. Fujisawa, B. Driesen, C.-H. Hsu, K. Kawaguchi, H. Tanaka, T. Kondo, Y. Zhang, H. Wadati, K. Araki, *et al.*, *Physical Review B* **103**, L060403 (2021).
- ³¹K. Yamagami, Y. Fujisawa, M. Pardo-Almanza, B. Smith, K. Sumida, Y. Takeda, and Y. Okada, *Physical Review B* **106**, 045137 (2022).
- ³²S. Ershadrad, N. Machacova, A. Mukherjee, V. Borisov, O. Eriksson, and B. Sanyal, *arXiv preprint arXiv:2504.00643* (2025).
- ³³S. Ghosh, S. Ershadrad, V. Borisov, and B. Sanyal, *npj Computational Materials* **9**, 86 (2023).
- ³⁴B. Marfoua and J. Hong, *NPG Asia Materials* **16**, 6 (2024).
- ³⁵V. Borisov, *Electronic Structure*, 023002 (2024).
- ³⁶V. Borisov, A. Delin, and O. Eriksson, *Physical Review B* **110**, L060407 (2024).
- ³⁷V. Borisov, N. Salehi, M. Pereiro, A. Delin, and O. Eriksson, *npj Computational Materials* **10**, 53 (2024).
- ³⁸S. Rohart and A. Thiaville, *Physical Review B* **88**, 184422 (2013).
- ³⁹J.-V. Kim and J. Mulkers, *IOP SciNotes* **1**, 025211 (2020).
- ⁴⁰W. Kohn and L. J. Sham, *Phys. Rev.* **140**, A1133 (1965).
- ⁴¹P. Hohenberg and W. Kohn, *Phys. Rev.* **136**, B864 (1964).
- ⁴²G. Kresse and J. Hafner, *Phys. Rev. B* **47**, 558 (1993).
- ⁴³G. Kresse and J. Hafner, *Phys. Rev. B* **49**, 14251 (1994).
- ⁴⁴G. Kresse and J. Furthmüller, *Comput. Mater. Sci.* **6**, 15 (1996).
- ⁴⁵G. Kresse and J. Furthmüller, *Phys. Rev. B* **54**, 11169 (1996).
- ⁴⁶J. P. Perdew, K. Burke, and M. Ernzerhof, *Phys. Rev. Lett.* **77**, 3865 (1996).
- ⁴⁷P. E. Blöchl, *Phys. Rev. B* **50**, 17953 (1994).
- ⁴⁸A. Togo and I. Tanaka, *Scr. Mater.* **108**, 1 (2015).
- ⁴⁹S. Smidstrup, T. Markussen, P. Vancraeyveld, J. Wellendorff, J. Schneider, T. Gunst, B. Verstichel, D. Stradi, P. A. Khomyakov, U. G. Vej-Hansen, *et al.*, *Journal of Physics: Condensed Matter* **32**, 015901 (2019).
- ⁵⁰M. J. Van Setten, M. Giantomassi, E. Bousquet, M. J. Verstraete, D. R. Hamann, X. Gonze, and G.-M. Rignanese, *Computer Physics Communications* **226**, 39 (2018).
- ⁵¹A. A. Mostofi, J. R. Yates, Y.-S. Lee, I. Souza, D. Vanderbilt, and N. Marzari, *Computer physics communications* **178**, 685 (2008).
- ⁵²X. He, N. Helbig, M. J. Verstraete, and E. Bousquet, *Computer Physics Communications* **264**, 107938 (2021).
- ⁵³A. I. Liechtenstein, M. Katsnelson, V. Antropov, and V. Gubanov, *Journal of Magnetism and Magnetic Materials* **67**, 65 (1987).
- ⁵⁴O. Eriksson, A. Bergman, L. Bergqvist, and J. Hellsvik, *Atomistic spin dynamics: foundations and applications* (Oxford university press, 2017).
- ⁵⁵A. Vansteenkiste, J. Leliaert, M. Dvornik, M. Helsen, F. Garcia-Sanchez, and B. Van Waeyenberge, *AIP Advances* **4**, 107133 (2014).
- ⁵⁶J. Mulkers, B. Van Waeyenberge, and M. V. Milošević, *Physical Review B* **95**, 144401 (2017).
- ⁵⁷J. J. Joos, P. Bassirian, P. Gypens, J. Mulkers, K. Litzius, B. Van Waeyenberge, and J. Leliaert, *Journal of Applied Physics* **134** (2023).
- ⁵⁸G. Henkelman, A. Arnaldsson, and H. Jónsson, *Comput. Mater. Sci.* **36**, 354 (2006).
- ⁵⁹H. Wu, S. Li, Y. Lyu, Y. Guo, W. Liu, J. S. Oh, Y. Zhang, S.-K. Mo, C. dela Cruz, R. J. Birgeneau, *et al.*, *Physical Review B* **109**, 174427 (2024).